Research Square

Preprints are preliminary reports that have not undergone peer review.
They should not be considered conclusive, used to inform clinical practice,
or referenced by the media as validated information.

Dehydrolithocholic acid–FBW7–c-Jun signaling in CD8⁺ T cell dysfunction in colorectal cancer

Xueyan Zhou

zxy851107@xzhmu.edu.cn

Xuzhou Medical University https://orcid.org/0000-0003-2821-1013

Jun Song

The Affiliated Hospital of Xuzhou Medical University https://orcid.org/0000-0002-6350-2695

lianyu liu

Xuzhou Medical University

Xuanzheng Zhou

Xuzhou Medical University

Qian Lu

The Affiliated Hospital of Xuzhou Medical University

Jingshan Tong

Xuzhou Medical University

Qianqian Duan

Xuzhou Medical University

Chuang Meng

Xuzhou Cancer Hospital

Chuting Huang

Xuzhou Medical University

Tianhong Li

Xuzhou Medical University

Article

Keywords: colorectal cancer, dehydrolithocholic acid, CD8⁺ T cells, c-Jun, FBW7

Posted Date: November 12th, 2026

DOI: https://doi.org/10.21203/rs.3.rs-11104418/v1

License: This work is licensed under a Creative Commons Attribution 4.0 International License.
Read Full License

Additional Declarations: (Not answered)

Dehydrolithocholic acid–FBW7–c-Jun signaling in CD8$^+$ T cell dysfunction in colorectal cancer

Lianyu Liu[1,2+], Xuanzheng Zhou[1+], Qian Lu[3], Jingshan Tong[1], Qianqian Duan[1], Chuang Meng[2], Chuting Huang[1], Tianhong Li[1], Jun Song[4]*, and Xueyan Zhou[1]*

[1] Jiangsu Key Laboratory of New Drug Research and Clinical Pharmacy, Xuzhou Medical University, Xuzhou, Jiangsu, China

[2] Department of Gastrointestinal Surgery, Xuzhou Cancer Hospital, Xuzhou, Jiangsu, China

[3] Department of Gastroenterology, The Affiliated Hospital of Xuzhou Medical University, Xuzhou, Jiangsu, China

[4] Institute of Digestive Diseases, Xuzhou Medical University, Xuzhou, Jiangsu, China

[+] These authors contributed equally to this work.

* Correspondence: Xueyan Zhou (primary corresponding author), zxy851107@xzhmu.edu.cn; Jun Song, songjun@xzhmu.edu.cn.

Running title: DHLCA-FBW7-c-Jun signaling in CD8$^+$ T cells

Abstract

Gut microbiota-derived bile acids can influence mucosal immunity, but their effects on antitumor $CD8^+$ T cells in colorectal cancer (CRC) are not well defined. Targeted fecal bile-acid profiling identified dehydrolithocholic acid (DHLCA) as enriched in treatment-naive patients with CRC and associated with more advanced clinicopathologic features. In syngeneic tumor models, oral DHLCA accelerated tumor growth, whereas this effect was no longer evident after $CD8^+$ T cell depletion. In primary mouse $CD8^+$ T cells, DHLCA reduced proliferation, IFN-γ and GzmB production, and antigen-specific tumor-cell killing; activated human $CD8^+$ T cells showed changes in the same direction. DHLCA lowered both *Jun* transcript abundance and c-Jun protein availability. Cycloheximide chase, proteasome inhibition, and immunoprecipitation experiments further showed faster c-Jun turnover together with increased FBW7-c-Jun association and c-Jun-associated ubiquitination. Loss of c-Jun was accompanied by reduced AP-1 activity, lower c-Jun occupancy at *Gzmb* and *Ifng* regulatory regions, and weaker TRE-dependent reporter activity. Enforced c-Jun expression partially restored $CD8^+$ T cell effector function and antitumor activity despite continued DHLCA exposure. DHLCA also weakened tumor control during PD-1 blockade. These results link a microbiota-associated bile acid to impaired $CD8^+$ T cell function through coordinated RNA-level and post-translational regulation of c-Jun.

Keywords: colorectal cancer; dehydrolithocholic acid; $CD8^+$ T cells; c-Jun; FBW7;

Introduction

Colorectal cancer (CRC) remains a major cause of cancer morbidity and mortality worldwide.[1] Clinical outcome is closely related to the abundance and spatial organization of tumor-infiltrating immune cells, particularly cytotoxic T lymphocytes.[2,3] Immune checkpoint blockade can produce durable responses in a subset of mismatch repair-deficient or microsatellite instability-high

tumors,[4,5] yet most patients with CRC receive little or no benefit. A central limitation is the progressive loss of $CD8^+$ T cell proliferative capacity and cytotoxic function within the tumor microenvironment.[6,7]

Gut microbial metabolism generates a chemically diverse pool of secondary bile acids, several of which directly affect immune-cell differentiation and function.[8–10] DHLCA (3-oxoLCA), an oxidized derivative of lithocholic acid, can suppress TH17 differentiation, and bacterial species and hydroxysteroid dehydrogenases capable of producing DHLCA have been described in the human gut.[8,11] Whether DHLCA also acts on cytotoxic $CD8^+$ T cells, and whether such an effect is relevant to CRC progression or treatment response, has remained unclear.

$CD8^+$ T cell activation depends on coordinated AP-1 and NFAT signaling; persistent NFAT activity in the absence of adequate AP-1 cooperation instead favors dysfunctional transcriptional programs.[7,12] c-Jun is an important AP-1 component, and increasing c-Jun expression can improve T cell proliferation, cytokine production, and resistance to exhaustion-like states.[13] Its abundance is tightly regulated by ubiquitin-dependent proteolysis, including recognition by the SCF substrate receptor FBW7.[14,15] This raised the possibility that a microbiota-derived metabolite might influence antitumor T cell function by altering c-Jun abundance rather than by acting only on receptor-proximal signaling.

We therefore examined DHLCA in clinical samples, primary $CD8^+$ T cells, and complementary mouse tumor models. DHLCA was elevated in CRC and suppressed $CD8^+$ T cell proliferation, effector-molecule production, and antigen-specific killing. At the molecular level, DHLCA lowered steady-state *Jun* mRNA while accelerating FBW7-associated proteasomal turnover of c-Jun, reducing the c-Jun pool available for AP-1-dependent transcription. c-Jun restoration partially reversed the functional defect in vitro and in vivo. We also tested the pathway

during PD-1 blockade and in activated human $CD8^+$ T cells to assess its therapeutic and translational relevance.

Materials and methods

Ethics, study participants, and experimental models

Fresh fecal samples were collected from newly diagnosed, treatment-naive patients with colorectal cancer (CRC) and healthy donors at Xuzhou Cancer Hospital between September 2023 and January 2026. CRC was confirmed by colonoscopic biopsy or surgical pathology according to the Chinese Guidelines for the Diagnosis and Treatment of Colorectal Cancer (2023 edition). Written informed consent was obtained from all participants. The study was approved by the Ethics Committee of Xuzhou Cancer Hospital (2023-CS-018).

CRC inclusion criteria were histopathologically confirmed CRC, first diagnosis without antitumor treatment before sample collection, clinicopathologic information sufficient for TNM staging, and written informed consent. Healthy donors had no known gastrointestinal disease, malignancy, or autoimmune disease and provided written informed consent. Exclusion criteria included use of aminosalicylates, glucocorticoids, immunosuppressants, biologic agents, antibiotics, probiotics, or bile-acid-related drugs before sample collection; inflammatory or infectious intestinal disease; gastrointestinal bleeding, perforation, fistula, or obstruction; severe cardiac, neurologic, hepatic, or renal dysfunction; pregnancy or lactation; psychiatric disease; incomplete clinical information; participation in another clinical trial; or receipt of antitumor treatment before sample collection.

Peripheral blood was collected from healthy donors into EDTA-anticoagulated tubes. Ten milliliters of blood from each donor were processed within 2 h of collection. Peripheral blood mononuclear cells (PBMCs) were isolated by Ficoll-Paque Premium density-gradient

centrifugation and used immediately for ex vivo activation experiments. For paired analyses, PBMCs from each donor were divided between vehicle and DHLCA conditions. All donors provided written informed consent, and the protocol was approved by the Ethics Committee of Xuzhou Cancer Hospital.

C57BL/6J, BALB/c, BALB/c nude, OT-1 transgenic, CD45.1^{+} OT-1 transgenic, and Apc$^{Min/+}$ mice were obtained from GemPharmatech Co., Ltd. Mice were maintained under specific pathogen-free conditions at the Experimental Animal Center of Xuzhou Medical University at 22 ± 2°C and 50% ± 5% relative humidity on a 12-h light/dark cycle, with free access to chow and water. All animal procedures were approved by the Animal Ethics Committee of Xuzhou Medical University (202602T006) and were performed in accordance with the approved protocol and relevant institutional guidelines and regulations. Male mice aged 6–8 weeks were used for MC38, CT26, nude-mouse, and OT-1 experiments; male Apc$^{Min/+}$ mice entered experiments at 6 weeks of age. Unless otherwise specified, *in vivo* experiments used n = 6 mice per group. The chronic Apc$^{Min/+}$ diet experiment used n = 7 control-diet mice and n = 8 DHLCA-diet mice. Animals were randomly assigned to experimental groups before intervention.

MC38, MC38-OVA, CT26, CT26-OVA, HCT116, HEK293T, and Jurkat cells were maintained as laboratory stocks. MC38, MC38-OVA, HCT116, and HEK293T cells were cultured in DMEM supplemented with 10% fetal bovine serum and 1% penicillin-streptomycin. CT26, CT26-OVA, and Jurkat cells were cultured in RPMI 1640 supplemented with 10% fetal bovine serum and 1% penicillin-streptomycin. Cells were maintained at 37°C in a humidified 5% CO2 incubator and were routinely screened for mycoplasma contamination.

Fecal sample collection and storage

Fasting fecal samples were collected before surgery or any other antitumor treatment. Samples were placed in sterile collection tubes, transported to the laboratory on ice within 2 h, aliquoted to minimize repeated freeze-thaw cycles, and stored at -80°C until targeted bile-acid analysis.

Targeted LC-MS/MS profiling of fecal bile acids

Fecal bile acids were quantified by matrix-matched targeted LC-MS/MS using dehydrocholic acid as the internal standard. Chromatographic separation was performed on an Agilent C18 column with ammonium acetate/acetonitrile mobile phases, and analytes were detected on an AB SCIEX AB5500 in negative-ion MRM mode. Concentrations were calculated from matrix-matched calibration curves after internal-standard normalization. Detailed extraction, calibration, and instrument procedures are provided in Supplementary Methods.

Fecal bile acid data processing

Peak areas were normalized to the internal standard and converted to absolute concentrations from matrix-matched calibration curves. Bile-acid features detected in fewer than 80% of all samples were excluded from the primary comparative analysis. Features retained for the primary analysis were visualized after $\log10(x + 1)$ transformation. Group comparisons were performed using two-sided Mann-Whitney U tests, and multiple testing was controlled with the Benjamini-Hochberg false-discovery-rate procedure.

Candidate bacterial analysis and fecal bacterial qPCR

Candidate DHLCA-producing species were nominated by reanalysis of the bacterial bile-acid transformation dataset reported by Paik et al.11 Eggerthella lenta, Gordonibacter pamelaeae, and Raoultibacter massiliensis were selected for fecal qPCR validation. Species-specific qPCR was performed on fecal bacterial DNA using primer sets listed in Table S2, and relative abundance was expressed as $-\Delta Ct$ values.

Subcutaneous tumor models

MC38 cells in logarithmic growth were harvested, washed with PBS, and resuspended in sterile PBS. C57BL/6J mice received a subcutaneous flank injection of 1×10^6 MC38 cells in 100 μL. Vehicle or DHLCA treatment began on day 1 after tumor inoculation. Tumor length and width were measured every 3 days with calipers, and tumor volume was calculated as length × width²/2. Tumors, spleens, and tumor-draining lymph nodes were collected at the prespecified study endpoint for weight measurement and immune analysis. CT26 tumors were established in BALB/c mice using 1×10^6 CT26 cells per mouse and were monitored using the same schedule. For the immunodeficient-host experiment, 1×10^6 MC38 cells were implanted subcutaneously into BALB/c nude mice and animals received the same vehicle or DHLCA dosing regimen beginning on day 1.

***In vivo* DHLCA administration**

DHLCA was formulated at 2 mg/mL in 10% DMSO, 40% PEG300, 5% Tween 80, and 45% PBS. Mice received DHLCA by oral gavage once daily at 10 mg/kg; vehicle-treated mice received the same volume of vehicle. The dosing solution was prepared fresh, protected from light, and used on the day of administration. Body weight and general health were monitored throughout treatment.

$CD8^+$ T cell depletion

For $CD8^+$ T cell depletion, MC38 tumor-bearing mice received 200 μg anti-mouse CD8α antibody or the corresponding isotype control by intraperitoneal injection on days -6, +1, and +8 relative to tumor inoculation. Depletion efficiency was assessed by flow cytometric measurement of CD8+ T cell frequencies.

Anti-PD-1 treatment model

For checkpoint-blockade experiments, C57BL/6J mice were implanted subcutaneously with MC38 cells. Vehicle or DHLCA administration began on day 1 after tumor inoculation. Mice received 200 μg anti-PD-1 antibody (clone RMP1-14) or isotype IgG by intraperitoneal injection on days 7 and 14. Experimental groups were vehicle + IgG, DHLCA + IgG, vehicle + anti-PD-1, and DHLCA + anti-PD-1. Tumor growth was monitored through day 21, when tumors and immune tissues were collected for flow-cytometric analysis.

Apc $^{Min/+}$ mouse model

Age-matched male Apc$^{Min/+}$ mice were randomly assigned to control diet (n = 7) or DHLCA-formulated diet (n = 8). The DHLCA diet was prepared to provide an estimated daily exposure of approximately 10 mg/kg based on expected food intake. Mice were followed until 120 days of age or until humane endpoints were reached. Survival, body weight, and grossly visible colonic lesion burden were recorded. Colonic lesions and lesion-associated immune cells were collected for downstream analysis. Because not all gross lesions were independently confirmed by histopathology, these endpoints are reported as visible colonic lesions rather than carcinomas.

Tumor tissue dissociation and enrichment of tumor-infiltrating immune cells

Tumors were mechanically minced, enzymatically dissociated, filtered, and enriched for tumor-infiltrating immune cells by discontinuous Percoll density-gradient centrifugation. Tumor-draining lymph nodes and spleens were processed into single-cell suspensions for downstream flow cytometry. Detailed procedures are provided in Supplementary Methods.

Flow cytometry

Single-cell suspensions were stained with viability dye and surface-antibody panels, followed where indicated by fixation/permeabilization and intracellular cytokine or transcription-factor staining. Data were acquired on a BD FACSCanto II and analyzed in FlowJo v10.9 after

sequential exclusion of debris, doublets, and nonviable cells. Detailed staining and stimulation procedures are provided in Supplementary Methods.

Primary mouse CD8$^+$ T cell isolation and activation

Spleens from C57BL/6J or OT-1 mice were mechanically dissociated to obtain single-cell suspensions. Naive CD8$^+$ T cells were isolated by negative selection using the MojoSort Mouse CD8 Naive T Cell Isolation Kit, and purity was verified by flow cytometry. Cells were cultured in RPMI 1640 supplemented with 10% fetal bovine serum, 1% penicillin-streptomycin, and IL-2 (10 ng/mL). For initial activation, anti-CD3ε and anti-CD28 were used at 1:500 and 1:1,000 dilutions of the stock solutions, respectively. Unless otherwise stated, 2×10^6 cells were cultured per well in 24-well plates. DHLCA was added at 0, 20, or 40 μM with matched DMSO (<0.1%). For 6-day functional assays, anti-CD3/anti-CD28 plus IL-2 were used during days 0–3, after which cells were maintained with IL-2 and IL-7 during days 3–6; vehicle or DHLCA was maintained throughout the culture period.

CD8$^+$ T cell proliferation assays

For CFSE assays, purified CD8$^+$ T cells were resuspended at 1×10^7 cells/mL and labeled with 2.5 μM CFSE for 10 min at 37°C protected from light. Labeling was terminated with four volumes of pre-cooled complete medium, followed by 5 min on ice and two PBS washes. Cells were then cultured at 1×10^6 cells/mL in 24-well plates with vehicle, 20 μM DHLCA, or 40 μM DHLCA for 72 h. CFSE mean fluorescence intensity (MFI) was quantified by flow cytometry as the proliferation-associated readout shown in Figure 3C. In parallel, Ki-67 staining was performed after 72 h of vehicle or DHLCA treatment, and Ki-67 MFI was quantified as shown in Figure 3D.

Intracellular cytokine staining

For 6-day cytokine and transcription-factor assays, $CD8^+$ T cells were activated with anti-CD3/anti-CD28 and IL-2 during days 0–3 and maintained with IL-2 and IL-7 during days 3–6, with vehicle or DHLCA present throughout. Cells were then restimulated for 4 h with PMA and ionomycin in the presence of brefeldin A and monensin. After surface staining, fixation, and permeabilization, intracellular IFN-γ, GzmB, T-bet, and Eomes were quantified by flow cytometry as indicated in the corresponding figures.

OT-1 cytotoxicity assay

OT-1 $CD8^+$ T cells were isolated from spleens and activated with anti-CD3/anti-CD28 and IL-2. Cells were exposed to vehicle or DHLCA and washed before co-culture to remove extracellular DHLCA. OT-1 cells were then co-cultured with MC38-OVA or CT26-OVA target cells at an effector-to-target ratio of 5:1 for 24 h. Target-cell death was measured by Annexin V/propidium iodide staining, and cytotoxicity was independently assessed using the LDH release assay.

CRC cell viability and proliferation assays

MC38 cells were treated with vehicle or DHLCA for the indicated durations. Cell viability was assessed by CCK-8 and proliferation by EdU incorporation, with results normalized to the corresponding vehicle control. Detailed procedures are provided in Supplementary Methods.

Bulk RNA-seq and analysis

Primary mouse $CD8^+$ T cells were activated for 6 days with vehicle or 40 μM DHLCA, with three independent biological replicates analyzed per condition, and collected for total RNA isolation. RNA quality assessment, library preparation, high-throughput sequencing, primary read quality control, alignment, and gene-level quantification were performed by a commercial sequencing service provider. Differential-expression analysis was performed using DESeq2. Genes with $|\log2 \text{ fold change}| > 0.25$ and nominal $P < 0.05$ were retained as an exploratory

candidate set, yielding 42 genes (10 upregulated and 32 downregulated) for cross-species integration with the human CRC single-cell dataset and subsequent qRT-PCR validation. FPKM values and differential-expression summary statistics, including fold change, log2 fold change, nominal P values, adjusted P values, and regulation direction, are provided in Table S3.

Human CRC scRNA-seq analysis

Public human CRC single-cell RNA-seq data (GSE144735) were obtained from GEO and analyzed in R using Seurat. Following quality control, normalization, dimensionality reduction, clustering, and cell-type annotation, immune cells were identified and T cells were subclustered to define $CD8^+$ T cell populations. Differential-expression analysis was restricted to tumor-derived versus normal-tissue-derived $CD8^+$ T cells. Border-region cells were displayed only for the visualization shown in Figure S4F and were not included in this differential-expression comparison. Mouse genes from the DHLCA-treated $CD8^+$ T cell RNA-seq candidate set were mapped to human orthologs, and genes showing concordant direction of change between the mouse dataset and the human tumor-versus-normal comparison were prioritized for validation.

qPCR

$CD8^+$ T cells were treated with 0, 20, or 40 μM DHLCA for 24, 48, or 72 h. Total RNA was isolated using the Super FastPure Cell RNA Isolation Kit and reverse transcribed using HiScript III RT SuperMix for RT-PCR. qPCR was performed with 2× ChamQ Universal SYBR qPCR Master Mix. Relative expression was calculated by the 2^−ΔΔCt method using Gapdh as the reference gene. Primer sequences are listed in Table S2.

Immunoblotting

Cells or tissues were lysed in RIPA buffer containing protease and phosphatase inhibitors, and protein concentration was measured by BCA assay. Equal amounts of protein were separated by

SDS-PAGE and transferred to membranes. Membranes were blocked with 5% BSA and incubated with primary antibodies overnight at 4°C, followed by HRP-conjugated secondary antibodies and chemiluminescent detection. Routine immunoblot signals were assessed qualitatively. Relative soluble-FBW7 profiles shown for the thermal-shift assay in Figure 6D and Figure 6E were derived from the soluble FBW7 immunoblot signal across the temperature series.

Cycloheximide chase assay

Activated $CD8^+$ T cells were pretreated with vehicle or DHLCA for 24 h before cycloheximide was added at a final concentration of 50 μM to inhibit new protein synthesis. Cells were collected at 0, 2, 4, 6, and 8 h after cycloheximide addition and analyzed by immunoblotting for c-Jun. The time-dependent c-Jun signal was compared qualitatively between vehicle- and DHLCA-treated conditions; no densitometric half-life calculation was performed.

Proteasome inhibition assay

For the c-Jun proteasome-rescue experiment shown in Figure 4E, activated $CD8^+$ T cells were treated with vehicle or DHLCA, and MG132 was added at a final concentration of 10 μM during the final 6 h before collection. For the FBW7 and c-Jun analysis shown in Figure 6A, activated primary $CD8^+$ T cells were exposed to vehicle or 40 μM DHLCA for 72 h, with 10 μM MG132 added only during the final 6 h where indicated. Cells were collected and analyzed by immunoblotting for FBW7 and c-Jun.

Immunoprecipitation and co-immunoprecipitation

Cells were lysed under non-denaturing conditions, and equal amounts of protein were incubated with the indicated antibody or a species-matched IgG control. Immune complexes were captured using Protein A/G magnetic beads, washed, eluted, and analyzed by immunoblotting. For c-Jun ubiquitin-associated signal analysis shown in Figure 4F, activated $CD8^+$ T cells were treated with

MG132 (10 μM) and PR-619 (10 μM) for the final 6 h before c-Jun immunoprecipitation. For the endogenous FBW7-c-Jun interaction shown in Figure 6B, activated primary $CD8^+$ T cells were exposed to vehicle or 40 μM DHLCA for 72 h, with MG132 (10 μM) added during the final 6 h where indicated, followed by c-Jun immunoprecipitation and FBW7 immunoblotting. For AP-1 complex analysis, c-Fos immunoprecipitates were probed for c-Jun.

ChIP-qPCR

Vehicle- or DHLCA-treated $CD8^+$ T cells were crosslinked with 1% formaldehyde for 10 min at room temperature and the reaction was quenched with glycine. Chromatin was sheared by sonication to an average fragment size of approximately 200–500 bp. ChIP was performed with a c-Jun antibody or matched IgG control using the Beyotime ChIP Assay Kit. After reverse crosslinking and DNA purification, qPCR was used to quantify c-Jun enrichment at TRE-containing regulatory regions of Gzmb and Ifng. Enrichment was expressed as percentage of input. ChIP-qPCR primer sequences are listed in Table S2.

Dual-luciferase reporter assay

Promoter fragments containing the predicted TRE sites from Gzmb or Ifng were cloned upstream of firefly luciferase, and matched reporters carrying mutations in the core TRE sequences were generated. HEK293T cells were seeded in 24-well plates and co-transfected with a wild-type or TRE-mutant firefly reporter, the pRL Renilla luciferase normalization vector, and either a c-Jun expression plasmid or empty vector. Firefly and Renilla luciferase activities were measured 24 h after transfection using the dual-luciferase reporter assay. Firefly activity was normalized to Renilla activity and then to the corresponding control condition. Reporter sequences are provided in Table S2.

Retroviral c-Jun overexpression in $CD8^+$ T cells

A retroviral vector driven by the MPSV promoter and co-expressing c-Jun and IRES-EGFP was generated. HEK293T cells were used for retroviral packaging. Primary mouse $CD8^+$ T cells were activated with anti-CD3/anti-CD28 and IL-2 for 24 h, transferred to RetroNectin-coated plates, and transduced with c-Jun-expressing or empty-control retrovirus. Transduction efficiency was quantified by EGFP expression. Transduced cells were then cultured with vehicle or 40 μM DHLCA for 72 h before immunoblotting, flow-cytometric functional analysis, or OT-1 cytotoxicity experiments.

Molecular docking

A structured human FBW7 core region (PDB ID: 2OVP) was used as the receptor model for docking. Water molecules and non-relevant ligands were removed, hydrogens and charges were assigned, and the three-dimensional DHLCA ligand was energy minimized. Docking was performed with AutoDock Vina v1.2, poses were ranked by predicted binding energy, and the top-ranked configurations were inspected in PyMOL v2.5 for pocket occupancy, polar contacts, and interatomic distances.

FBW7 pocket mutant construction

Based on the docking-defined distal pocket, six candidate FBW7 residues were selected for mutagenesis: I330, D331, R357, K590, F632, and N668. For each position, the corresponding wild-type codon was replaced with the alanine codon GCC, generating the six-site alanine-substitution construct FBW7-Mut. All six substitutions were introduced into the same Flag-tagged FBW7 expression construct by site-directed mutagenesis. The complete mutant coding sequence was verified by Sanger sequencing before use. Wild-type and mutant FBW7 coding sequences and mutagenic primer sequences are provided in Table S2.

Lysate-based thermal shift assay

HEK293T cells were transfected with wild-type or pocket-mutant FBW7 expression plasmids. Cell lysates were incubated with vehicle or 40 μM DHLCA for 2 h, aliquoted, and heated at 49, 52, 55, 58, 61, or 64°C for 20 min. Samples were then centrifuged to remove heat-precipitated protein, and residual soluble Flag-FBW7 in the supernatant was assessed by immunoblotting. Relative soluble-FBW7 signal across the temperature series was plotted as shown in Figure 6D and Figure 6E.

Reconstituted FBW7-c-Jun interaction assay in HEK293T cells

HEK293T cells were co-transfected with c-Jun and either Flag-tagged wild-type FBW7 or the six-site alanine pocket mutant. Cells were exposed to vehicle or 40 μM DHLCA for 24 h. For the interaction experiments shown in Figures 6F and 6G, MG132 (10 μM) and PR-619 (10 μM) were added during the final 6 h before cell collection. Cells were lysed under non-denaturing conditions, and Flag-FBW7 complexes were immunoprecipitated using an anti-Flag antibody followed by immunoblotting for c-Jun and Flag-FBW7. For the protein-abundance experiments shown in Figures 6H and 6I, cells expressing wild-type or pocket-mutant FBW7 were treated with vehicle or 40 μM DHLCA for 24 h without MG132/PR-619 treatment, and c-Jun and FBW7 abundance was assessed in whole-cell lysates by immunoblotting.

OT-1 adoptive transfer model

MC38-OVA tumors were established in syngeneic C57BL/6J recipient mice by subcutaneous inoculation of 2×10^6 MC38-OVA cells. $CD45.1^+$ OT-1 $CD8^+$ T cells were transduced with empty-control or c-Jun expression vectors and exposed ex vivo to vehicle or DHLCA. On days 7 and 14 after tumor inoculation, each mouse received 1×10^6 treated $CD45.1^+$ OT-1 cells by intravenous injection. Tumor growth was monitored through day 21. At endpoint, tumor weight

was recorded and transferred OT-1 cells were analyzed for donor-cell frequency and expression of c-Jun, IFN-γ, and GzmB.

Human PBMC activation and DHLCA treatment

Fresh PBMCs from 12 healthy donors were divided into paired vehicle and DHLCA conditions. Cells were activated ex vivo with the same anti-CD3ε and anti-CD28 reagents listed in the Key Resources Table together with IL-2 during days 0–3. During days 3–6, cells were maintained with IL-2 and IL-7. Vehicle or 40 μM DHLCA was present throughout the 6-day culture period. After PMA/ionomycin restimulation, GzmB and IFN-γ were measured in $CD8^+$ T cells. Flow cytometry was also used to quantify the frequency of $CD8^+$ T cells within $CD3^+$ T cells and c-Jun expression in $CD8^+$ T cells, with c-Jun reported as mean fluorescence intensity in Figure 7Q. Vehicle- and DHLCA-treated aliquots from the same donor were analyzed as paired samples.

Quantification and statistical analysis

Statistical analyses were performed using GraphPad Prism v9.5, SPSS v25.0, and R v4.2. Data are presented as mean ± SD, mean ± SEM, or median with interquartile range, as specified in each figure legend. The individual participant was the experimental unit for human studies, the individual mouse for *in vivo* studies, and an independently prepared biological sample for *in vitro* experiments. Unless otherwise indicated, *in vitro* experiments were performed as three independent biological experiments (n = 3), and mouse experiments used n = 6 mice per group. The chronic $Apc^{Min/+}$ diet experiment used n = 7 control-diet mice and n = 8 DHLCA-diet mice. Technical replicate wells were summarized within each biological replicate before inferential testing. Two independent groups were compared using a two-sided unpaired Student's t test for normally distributed data or a two-sided Mann-Whitney U test for nonparametric data. Pearson's χ^2 test or Fisher's exact test was used for clinical correlation analysis. Paired PBMC comparisons

were analyzed using a paired t test or Wilcoxon matched-pairs signed-rank test according to data distribution. One-factor experiments were analyzed by one-way ANOVA followed by Dunnett's test for comparisons against a single control or Tukey's test for all pairwise comparisons. Two-factor experiments were analyzed by two-way ANOVA followed by Šídák-adjusted planned comparisons; the dual-luciferase experiments were modeled with reporter genotype and c-Jun expression as factors. Longitudinal tumor-growth data were analyzed by two-way repeated-measures ANOVA when complete repeated measurements were available and by a mixed-effects model when values were missing. Survival curves were estimated by the Kaplan-Meier method and compared by log-rank test. Correlations were assessed by Spearman rank correlation. Bile-acid profiling P values were adjusted by the Benjamini-Hochberg false-discovery-rate method. All tests were two-sided unless otherwise stated, and $P < 0.05$ was considered statistically significant.

Resource and data availability

Further information and requests for resources and reagents should be directed to Xueyan Zhou (zxy851107@xzhmu.edu.cn). Unique reagents generated in this study are available from the corresponding author upon reasonable request and subject to institutional material-transfer requirements.

Bulk RNA-seq data generated in this study will be deposited in a public repository before publication. The public human CRC single-cell RNA-seq dataset analyzed in this study is available from GEO under accession GSE144735. This study does not report original software. Additional information required to reanalyze the data is available from the corresponding author upon reasonable request.

Use of generative AI in manuscript preparation

ChatGPT (OpenAI) was used for language editing, condensation, and journal-formatting assistance. All scientific content, data interpretation, and final wording were reviewed and approved by the authors.

Results

Fecal DHLCA is enriched in colorectal cancer and associated with disease progression

We first profiled fecal bile acids in 77 newly diagnosed, treatment-naive patients with CRC and 29 healthy donors by targeted LC-MS/MS. Age, sex, and body mass index were comparable between groups (Table S1). Of 41 bile acid standards included in the assay, 38 bile acid or derivative signals were detected across the cohort (Figure S1A). Eighteen features were present in >80% of the 106 samples and were carried forward for the primary comparison (Figure S1B). After Benjamini-Hochberg correction, several bile acid features differed between CRC and control feces (Figure 1B). DHLCA showed one of the clearest differences: the median concentration was 163 ng/mL (IQR, 115–211) in CRC and 89.5 ng/mL (IQR, 73.7–126) in healthy donors, with a 1.66-fold increase in mean abundance ($P = 1.07 \times 10^{-4}$; Figure 1C).

Higher fecal DHLCA was also associated with more advanced disease. Concentrations were greater in T3–T4 than T1–T2 tumors, N1–N2 than N0 disease, M1 than M0 cases, and stage III–IV than stage I–II CRC (Figures 1D–1G). Using the cohort median as the cutoff, the high-DHLCA group was enriched for deeper invasion, lymph-node involvement, distant metastasis, and advanced TNM stage, whereas age, sex, tumor size, and histologic differentiation did not differ significantly (Table 1).

Published bacterial bile-acid transformation data were then used to nominate possible microbial contributors to the DHLCA pool.11 E. lenta, G. pamelaeae, and R. massiliensis were selected as candidate 3-oxoLCA-producing species (Figure S7A). Fecal qPCR showed that E.

lenta, but not the other two candidates, was enriched in CRC (Figures S7B–S7D). E. lenta abundance correlated with fecal DHLCA and was higher in patients with more advanced T, N, and M categories and TNM stage (Figures S7E–S7I). These clinical associations point to E. lenta as a possible contributor to the DHLCA-enriched state, but they do not establish that it is the causal or exclusive source in vivo.

DHLCA promotes colorectal tumor growth through a $CD8^+$ T cell-dependent mechanism

We next asked whether the clinical association between DHLCA and advanced CRC had a functional counterpart in vivo. In BALB/c nude mice bearing MC38 tumors, daily oral DHLCA (10 mg/kg) from day 1 did not significantly change tumor growth or terminal tumor weight (Figures S2A–S2D). DHLCA likewise failed to increase MC38 viability or proliferation in CCK-8 and EdU assays (Figures S2E and S2F). Under these conditions, a strong tumor-cell-intrinsic proliferative effect was therefore unlikely.

The outcome differed in immunocompetent hosts. In C57BL/6J mice bearing syngeneic MC38 tumors, the same DHLCA regimen accelerated tumor growth and increased final tumor weight (Figures 2A–2D). A similar increase in tumor burden was observed in BALB/c mice bearing CT26 tumors (Figures S2G–S2J). The contrast with the nude-mouse and in vitro experiments pointed to an immune-dependent component of the DHLCA effect.

Flow cytometry at endpoint showed fewer $CD8^+$ T cells within the intratumoral $CD3^+$ compartment after DHLCA treatment (Figure 2E). Tumor-draining lymph nodes showed a smaller decrease in $CD8^+$ T cells and a reciprocal increase in $CD4^+$ T cells, while macrophage, B-cell, and NK-cell frequencies changed little (Figures 2F–2L). Splenic immune composition was largely unchanged (Figures S2O–S2R). The CT26 model showed a similar pattern, with

fewer intratumoral $CD8^+$ T cells and a relative increase in $CD4^+$ T cells but no broad shift in the other leukocyte populations examined (Figures S2K–S2N).

$CD8^+$ T cell depletion was used to test whether this compartment was required for tumor promotion by DHLCA. MC38-bearing mice received anti-CD8α or isotype control together with vehicle or DHLCA (Figure 2M), and depletion was verified by flow cytometry (Figure 2N). In IgG-treated mice, DHLCA increased both tumor growth and terminal burden. Once $CD8^+$ T cells were depleted, tumor control was already impaired and the difference between vehicle and DHLCA was lost (Figures 2O–2Q), indicating that the protumor effect of DHLCA depends largely on $CD8^+$ T cells.

DHLCA suppresses $CD8^+$ T cell proliferation and cytotoxic effector function with limited changes in selected exhaustion-associated receptors

Because intratumoral $CD8^+$ T cells were reduced in vivo, we examined whether DHLCA directly affected activated $CD8^+$ T cells. Purified splenic $CD8^+$ T cells were stimulated with anti-CD3/anti-CD28 and IL-2 and exposed to 0, 20, or 40 μM DHLCA (Figure 3A). CFSE dilution and Ki-67 staining at 72 h both showed a dose-related restraint on proliferative expansion (Figures 3C and 3D).

The effect extended to the effector program. During 6-day cultures, DHLCA reduced GzmB and IFN-γ in a concentration-dependent manner and also lowered T-bet and Eomes (Figures 3E–3H). Activated OT-1 cells showed the same reduction in GzmB and IFN-γ (Figures 3I and 3J). In the MC38 and CT26 models, tumor-associated and draining-lymph-node $CD8^+$ T cells likewise expressed less GzmB and IFN-γ after DHLCA exposure (Figures S3A–S3H).

Functional killing was assessed after DHLCA-pretreated OT-1 cells were washed and co-cultured with OVA-expressing target cells. Pretreatment reduced target-cell Annexin

V/propidium iodide positivity and LDH release (Figure 3B; Figures S3L–S3N). Repeated stimulation did not, however, produce a uniform increase in exhaustion-associated receptors: PD-1 and LAG-3 rose modestly at 40 μM DHLCA, whereas TIM-3 was unchanged (Figures S3I–S3K). The phenotype was therefore characterized more clearly by impaired expansion and cytotoxic output than by a coordinated inhibitory-receptor profile.

DHLCA reduces Jun transcript abundance, destabilizes c-Jun, and impairs AP-1-dependent effector transcription in CD8$^+$ T cells

To look for molecular changes associated with this functional defect, we performed RNA-seq on activated C57BL/6J CD8$^+$ T cells cultured for 6 days with vehicle or 40 μM DHLCA (n = 3 independent biological replicates per condition; Table S3). At exploratory thresholds of |log2 fold change| > 0.25 and nominal $P < 0.05$, DESeq2 retained 42 genes (10 upregulated and 32 downregulated; Figure S4A). Twenty-four had identifiable human orthologs. In the GSE144735 CRC single-cell dataset, 753 genes differed between tumor-derived and normal-tissue-derived CD8$^+$ T cells (Figures S4B and S4C). Ten transcripts changed in the same direction in both analyses (Figure 4A).

qPCR across 24, 48, and 72 h and at 0, 20, and 40 μM DHLCA narrowed this set further. *Jun* showed the most consistent and sustained decrease, whereas the remaining candidates varied more across dose and time (Figure 4B; Figures S4D and S4E). *JUN* expression was also lower in tumor-associated CD8$^+$ T cells than in normal-tissue counterparts in the public human single-cell dataset (Figure S4F).

At the protein level, DHLCA reduced total c-Jun in a dose-dependent manner and also lowered phosphorylated c-Jun. Total JNK, phospho-JNK, and c-Fos did not show a comparable decrease

(Figure 4C). This pattern was more consistent with loss of c-Jun abundance than with a primary block in proximal JNK activation.

Protein-stability experiments provided a second layer of evidence. After 24 h of DHLCA pretreatment, c-*Jun* declined more rapidly during cycloheximide chase (Figure 4D), and MG132 partially restored c-*Jun* despite continued DHLCA exposure (Figure 4E). DHLCA also increased ubiquitin immunoreactivity in c-*Jun* immunoprecipitates after MG132/PR-619 treatment; the same direction of change was seen in Jurkat cells (Figure 4F; Figure S4G). Thus, the fall in c-*Jun* reflects at least two detectable processes: lower steady-state *Jun* mRNA and faster proteasome-dependent turnover of the protein.

The reduced c-*Jun* pool had clear transcriptional consequences. c-Fos immunoprecipitates contained less c-*Jun* after DHLCA treatment despite preserved total c-Fos, consistent with fewer c-*Jun*-containing AP-1 complexes (Figure 4G). ChIP-qPCR showed lower c-*Jun* occupancy at two TRE-containing *Gzmb* regions and one *Ifng* region (Figures 4H–4K). In dual-luciferase assays, c-*Jun* activated the wild-type *Gzmb* and *Ifng* reporters, while mutation of the predicted TRE elements substantially weakened this response (Figures 4L and 4M). These experiments connect c-*Jun* loss with impaired AP-1-dependent transcription of key cytotoxic effector genes.

Restoring c-Jun partially rescues DHLCA-imposed defects in CD8$^+$ T cell function

To test whether the decrease in c-Jun was functionally important, primary mouse CD8$^+$ T cells were transduced with c-Jun-IRES-EGFP or matched control retrovirus before exposure to vehicle or 40 μM DHLCA. Approximately 70% of cells were EGFP$^+$ after transduction (Figure S5A), allowing direct comparison of four treatment groups.

In control-vector cells, DHLCA reduced both total and phosphorylated c-Jun. Enforced c-Jun expression restored the c-Jun pool despite continued DHLCA exposure, without an obvious

increase in upstream JNK signaling (Figure 5A). This restoration was functional but incomplete: c-Jun overexpression increased GzmB$^+$ and IFN-γ^+ CD8$^+$ T cell frequencies and partially recovered antigen-specific OT-1 killing (Figures 5B–5E; Figures S5B and S5C).

We also examined whether the same signaling effect was evident in tumor cells themselves. DHLCA did not reproducibly suppress the JNK-c-Jun-c-Fos axis or enhance proliferation in MC38, CT26, or HCT116 cells under the conditions tested (Figure S5D). This difference supports a functionally relevant role for c-Jun loss in CD8$^+$ T cells rather than a general effect on the pathway across cell types.

A distal pocket in FBW7 contributes to DHLCA-enhanced recognition of c-Jun

Because FBW7 is a recognized substrate receptor for c-Jun, we asked whether it contributed to the DHLCA-associated loss of c-Jun. Activated primary CD8$^+$ T cells were treated with vehicle or 40 μM DHLCA for 72 h, with MG132 added during the final 6 h where indicated. Total FBW7 changed little, whereas proteasome inhibition partially preserved c-Jun (Figure 6A). c-Jun immunoprecipitation showed greater endogenous FBW7-c-Jun association after DHLCA exposure (Figure 6B).

Docking against the structured core of human FBW7 suggested a low-energy pocket away from the canonical substrate-recognition surface (Figure 6C). To probe this region experimentally, we generated a six-site alanine mutant (I330A/D331A/R357A/K590A/F632A/N668A). In lysate-based thermal-shift assays, DHLCA increased the soluble thermal-stability profile of wild-type FBW7, whereas the shift was attenuated with the pocket mutant (Figures 6D and 6E).

We then tested the same pocket in a reconstituted HEK293T system. DHLCA increased the association of c-Jun with wild-type FBW7 after 24 h, while the six-site mutation weakened this

increase without abolishing basal recognition (Figures 6F and 6G). In cells analyzed without MG132/PR-619, DHLCA also reduced c-Jun more efficiently in the presence of wild-type than mutant FBW7 (Figures 6H and 6I). These experiments implicate the distal pocket in DHLCA-enhanced recognition of c-Jun, but they do not demonstrate direct binding between purified DHLCA and FBW7.

DHLCA impairs c-Jun-dependent antitumor immunity *in vivo* and limits tumor control

We next asked whether restoring c-Jun could improve the activity of tumor-reactive T cells in vivo. MC38-OVA tumors were established in congenic C57BL/6J recipients, and OT-1 cells expressing empty vector or c-Jun were exposed ex vivo to vehicle or DHLCA before transfer on days 7 and 14 (Figure 7A).

Mice receiving DHLCA-pretreated control OT-1 cells showed poorer tumor control than those receiving vehicle-pretreated control cells. c-Jun overexpression improved tumor control and partly offset the defect caused by DHLCA (Figures 7B–7D). Congenic tracking also showed fewer donor CD45.1$^+$ OT-1 cells within the tumor CD8$^+$ compartment after DHLCA exposure, whereas c-Jun overexpression partially restored donor-cell persistence together with c-Jun, IFN-γ, and GzmB expression (Figures S6A–S6D).

The pathway was also examined during PD-1 blockade. MC38-bearing mice received daily vehicle or DHLCA from day 1 and anti-PD-1 or isotype IgG on days 7 and 14 (Figure 7E). Anti-PD-1 reduced tumor growth, but tumor control was weaker in DHLCA-treated mice, which showed faster longitudinal growth and greater terminal tumor weight (Figures 7F–7H). During therapy, DHLCA was also associated with fewer CD8$^+$ T cells and lower c-Jun, IFN-γ, and GzmB expression in tumors and draining lymph nodes (Figures S6E–S6L), and it partly reversed the anti-PD-1-associated changes in PD-1 and TIM-3 (Figures S6M and S6N).

In a genetically driven setting, male ApcMin/+ mice were exposed to a DHLCA-containing diet from 6 weeks of age and followed until 120 days or a humane endpoint (Figure 7I). DHLCA increased the number of grossly visible colonic lesions and shortened survival (Figures 7J–7L). Lesion-associated $CD8^+$ T cells were less abundant and expressed lower IFN-γ and GzmB (Figures S6O–S6Q). The same overall phenotype was therefore evident in adoptive-transfer, checkpoint-blockade, and genetically driven intestinal tumor models.

DHLCA suppresses human $CD8^+$ T cell effector responses

We finally asked whether the main $CD8^+$ T cell phenotype could be reproduced in human cells. PBMCs from 12 healthy donors were activated ex vivo with anti-CD3, anti-CD28, and IL-2 during days 0–3 and maintained with IL-2 and IL-7 during days 3–6; paired aliquots received vehicle or 40 μM DHLCA throughout (Figure 7M). DHLCA reduced the fraction of $CD8^+$ T cells within the $CD3^+$ compartment and lowered GzmB, IFN-γ, and c-Jun expression after restimulation (Figures 7N–7Q). Thus, the principal changes observed in mouse $CD8^+$ T cells were also detectable in activated human cells.

Discussion

Our data place DHLCA at the intersection of microbial bile-acid metabolism and $CD8^+$ T cell dysfunction in CRC. Fecal DHLCA was higher in treatment-naive patients with CRC and was associated with more advanced disease. In experimental models, DHLCA restricted $CD8^+$ T cell expansion and cytotoxic function, promoted tumor growth in a $CD8^+$ T cell-dependent manner, and weakened tumor control during PD-1 blockade. The molecular data point to loss of the c-Jun pool as a key event: DHLCA lowered steady-state *Jun* mRNA while increasing FBW7-c-Jun association, c-Jun-associated ubiquitination, and proteasome-dependent turnover. Reduced c-Jun in turn limited AP-1-dependent transcription of *Gzmb* and *Ifng*. The partial rescue achieved by

restoring c-Jun argues that this transcription factor is functionally involved rather than serving only as a marker of DHLCA exposure.

The result fits with a growing view of bile acids as distinct signaling metabolites rather than a single functional class. Their immune effects vary with chemical structure, target cell, and anatomical compartment. Cong et al. reported that microbiota-modified bile acids can promote CRC by suppressing $CD8^+$ T cell function through Ca^{2+}-NFAT2 signaling,[16] and recent work has emphasized the context dependence of bile-acid signaling in cancer.[17] DHLCA appears to act through a different transcriptional route, centered on c-Jun and AP-1. The persistence of poorer tumor control during PD-1 blockade is consistent with the idea that checkpoint therapy cannot fully compensate for metabolic constraints imposed downstream or in parallel to receptor-proximal signaling.[18] Different bile acids may therefore reach a similar functional endpoint—weak cytotoxic T cell activity—through different molecular mechanisms.

A notable feature of the present data is that c-Jun falls at both the RNA and protein levels. The *Jun* locus is positively autoregulated by Jun/AP-1,[19] so depletion of the c-Jun protein pool could plausibly weaken this feedback and contribute to the later decline in steady-state *Jun* mRNA. At the same time, small molecules can change E3 ligase-substrate interactions without altering ligase abundance,[20] and c-Jun is a short-lived protein whose stability is controlled by ubiquitin-dependent degradation, multisite phosphorylation, and FBW7-dependent recognition.[21–25] The cycloheximide, MG132, ubiquitination, and FBW7-association experiments therefore support a genuine post-translational component of DHLCA action. They do not, however, show that protein turnover is the only cause of c-Jun loss. The temporal relationship between the RNA-level and protein-level effects remains unresolved, and DHLCA may influence *Jun* transcription or mRNA stability through an additional pathway.

The transcriptional consequences are consistent with established AP-1 biology. c-Jun/ATF2-containing complexes can regulate the *c-jun* promoter,[26] while AP-1 activity depends on dimer composition, post-translational modification, protein stability, and cellular context.[27–29] NFAT and Fos-Jun complexes also cooperate directly at composite immune-response elements.[30] In our experiments, DHLCA reduced c-Jun-c-Fos complex formation, c-Jun occupancy at *Gzmb* and *Ifng* regulatory regions, and TRE-dependent reporter activity. Notably, this was not accompanied by a uniform increase in PD-1, LAG-3, and TIM-3. The DHLCA-associated state is therefore not well described by inhibitory-receptor expression alone.

The FBW7 mutational experiments provide a structural clue, although the mechanism is not yet resolved at the level of direct binding. The six-site pocket mutant reduced the DHLCA-associated thermal-stability shift, weakened the increase in FBW7-c-Jun association, and lessened the effect of DHLCA on c-Jun abundance. This behavior is compatible with emerging concepts of ligand-induced modulation of E3 ligase specificity and targeted protein degradation,[31] but the current evidence does not justify classifying DHLCA as a molecular glue. Direct binding studies with purified components, quantitative measurements of ternary-complex formation, and endogenous FBW7 loss-and-rescue experiments in primary $CD8^+$ T cells will be needed to distinguish direct allosteric engagement from an indirect cellular mechanism.

The microbiome is a plausible upstream source of this signal, but the clinical data remain associative. Reanalysis of published bile-acid transformation data identified E. lenta, G. pamelaeae, and R. massiliensis as candidate DHLCA-producing organisms,[11] and fecal E. lenta was enriched in CRC, correlated with DHLCA, and increased with disease progression. Strain-specific enzymatic capacity, substrate availability, intestinal transit, and host metabolism can all influence fecal bile-acid levels, so these observations do not establish E. lenta as the in vivo

source of DHLCA. More broadly, lipid-derived metabolites can shape $CD8^+$ T cell differentiation and effector function in tumors,[32] and dysfunctional T cell states are multidimensional rather than defined solely by inhibitory receptors.[33] Their transcriptional and epigenetic stability may also limit the extent of reinvigoration achieved with PD-1 blockade.[34] From a therapeutic perspective, this argues for selective interference with DHLCA production or sensing rather than nonspecific depletion of the bile-acid pool.

Several limitations temper the mechanistic interpretation. Fecal DHLCA does not necessarily reflect the concentration encountered by tumor-infiltrating lymphocytes, and paired intratumoral metabolomics were not available. The clinical association with E. lenta also does not establish microbial causality. In primary $CD8^+$ T cells, endogenous FBW7 has not yet been genetically depleted, direct physical binding between DHLCA and FBW7 remains unproven, and cell-type-specific DHLCA uptake within the tumor microenvironment was not systematically measured. We also cannot determine from the present experiments whether the decline in *Jun* mRNA follows loss of c-Jun-dependent autoregulation or arises through a separate RNA-level mechanism. Even with these limitations, the clinical, cellular, biochemical, rescue, and in vivo data consistently converge on reduced c-Jun availability as a mechanism by which DHLCA can impair antitumor $CD8^+$ T cell function in CRC.

Data availability

Bulk RNA-seq data generated in this study will be deposited in a public repository before publication. The public human CRC single-cell RNA-seq dataset analyzed in this study is available from GEO under accession GSE144735. Additional information required to reanalyze the data is available from the corresponding author upon reasonable request.

Funding

This work was supported by the National Natural Science Foundation of China (No. 82173883), the Administration of Traditional Chinese Medicine of Jiangsu Province (No. MS2023175), and the Science and Technology Foundation of Xuzhou (No. KC23255).

Author contributions

Lianyu Liu and Xuanzheng Zhou contributed equally to this work. Lianyu Liu contributed to study conception and design, methodology development, investigation, data acquisition, formal analysis, data visualization, and preparation of the original manuscript. Xuanzheng Zhou contributed to methodology development, investigation, data acquisition, validation, formal analysis, and data visualization, and participated in manuscript preparation and revision. Qian Lu contributed to clinical sample collection, clinical data curation, and validation. Jingshan Tong contributed to methodology, investigation, and data analysis. Qianqian Duan contributed to investigation, validation, and data curation. Chuang Meng contributed to patient recruitment, clinical sample collection, and clinical data curation. Chuting Huang contributed to investigation, data curation, and visualization. Tianhong Li contributed to methodology, validation, and data interpretation. Jun Song contributed to study conception, supervision, resources, and critical revision of the manuscript. Xueyan Zhou contributed to study conception and design, project administration, supervision, resources, funding acquisition, interpretation of the data, and critical revision of the manuscript. All authors reviewed and approved the final manuscript.

Acknowledgements

We are grateful to all members of Jiangsu Key Laboratory of New Drug Research and Clinical Pharmacy for their technical support and valuable discussions. We also thank Xuzhou Cancer Hospital for assistance with patient recruitment, clinical sample collection, and clinical data acquisition.

Competing interests

The authors declare no competing interests.

References

1. Bray F, Laversanne M, Sung H, Ferlay J, Siegel RL, Soerjomataram I, et al. Global cancer statistics 2022: GLOBOCAN estimates of incidence and mortality worldwide for 36 cancers in 185 countries. CA Cancer J Clin. 2024;74:229–263. doi:10.3322/caac.21834.

2. Galon J, Costes A, Sanchez-Cabo F, Kirilovsky A, Mlecnik B, Lagorce-Pagès C, et al. Type, density, and location of immune cells within human colorectal tumors predict clinical outcome. Science. 2006;313:1960–1964. doi:10.1126/science.1129139.

3. Pagès F, Mlecnik B, Marliot F, Bindea G, Ou FS, Bifulco C, et al. International validation of the consensus Immunoscore for the classification of colon cancer: a prognostic and accuracy study. Lancet. 2018;391:2128–2139. doi:10.1016/S0140-6736(18)30789-X.

4. Le DT, Uram JN, Wang H, Bartlett BR, Kemberling H, Eyring AD, et al. PD-1 blockade in tumors with mismatch-repair deficiency. N Engl J Med. 2015;372:2509–2520. doi:10.1056/NEJMoa1500596.

5. André T, Shiu KK, Kim TW, Jensen BV, Jensen LH, Punt C, et al. Pembrolizumab in microsatellite-instability-high advanced colorectal cancer. N Engl J Med. 2020;383:2207–2218. doi:10.1056/NEJMoa2017699.

6. Blank CU, Haining WN, Held W, Hogan PG, Kallies A, Lugli E, et al. Defining T cell exhaustion. Nat Rev Immunol. 2019;19:665–674. doi:10.1038/s41577-019-0221-9.

7. Philip M, Schietinger A. $CD8^+$ T cell differentiation and dysfunction in cancer. Nat Rev Immunol. 2022;22:209–223. doi:10.1038/s41577-021-00574-3.

8. Hang S, Paik D, Yao L, Kim E, Trinath J, Lu J, et al. Bile acid metabolites control TH17 and Treg cell differentiation. Nature. 2019;576:143–148. doi:10.1038/s41586-019-1785-z.

9. Campbell C, McKenney PT, Konstantinovsky D, Isaeva OI, Schizas M, Verter J, et al. Bacterial metabolism of bile acids promotes generation of peripheral regulatory T cells. Nature. 2020;581:475–479. doi:10.1038/s41586-020-2193-0.

10. Collins SL, Stine JG, Bisanz JE, Okafor CD, Patterson AD. Bile acids and the gut microbiota: metabolic interactions and impacts on disease. Nat Rev Microbiol. 2023;21:236–247. doi:10.1038/s41579-022-00805-x.

11. Paik D, Yao L, Zhang Y, Bae S, D'Agostino GD, Zhang M, et al. Human gut bacteria produce TH17-modulating bile acid metabolites. Nature. 2022;603:907–912. doi:10.1038/s41586-022-04480-z.

12. Martinez GJ, Pereira RM, Äijö T, Kim EY, Marangoni F, Pipkin ME, et al. The transcription factor NFAT promotes exhaustion of activated $CD8^+$ T cells. Immunity. 2015;42:265–278. doi:10.1016/j.immuni.2015.01.006.

13. Lynn RC, Weber EW, Sotillo E, Gennert D, Xu P, Good Z, et al. c-Jun overexpression in CAR T cells induces exhaustion resistance. Nature. 2019;576:293–300. doi:10.1038/s41586-019-1805-z.

14. Zhang J, Zhu F, Li X, Tao K, Liu J, Wang G, et al. RACK1 protects N-terminal phosphorylated c-Jun from Fbw7-mediated degradation. Oncogene. 2012;31:1835–1844. doi:10.1038/onc.2011.369.

15. Davis RJ, Welcker M, Clurman BE. Tumor suppression by the Fbw7 ubiquitin ligase: mechanisms and opportunities. Cancer Cell. 2014;26:455–464. doi:10.1016/j.ccr.2014.09.013.

16. Cong J, Liu P, Han Z, Ying W, Li C, Yang Y, et al. Bile acids modified by the intestinal microbiota promote colorectal cancer growth by suppressing $CD8^+$ T cell effector functions. Immunity. 2024;57:876–889.e11. doi:10.1016/j.immuni.2024.02.014.

17. Fang Q, Schneider KM. Bile acids in cancer: From metabolism to immunomodulation. Immunity. 2026;59:2067–2085. doi:10.1016/j.immuni.2026.07.003.

18. Sharma P, Hu-Lieskovan S, Wargo JA, Ribas A. Primary, adaptive, and acquired resistance to cancer immunotherapy. Cell. 2017;168:707–723. doi:10.1016/j.cell.2017.01.017.

19. Angel P, Hattori K, Smeal T, Karin M. The jun proto-oncogene is positively autoregulated by its product, Jun/AP-1. Cell. 1988;55:875–885. doi:10.1016/0092-8674(88)90143-2.

20. Simonetta KR, Taygerly J, Boyle K, Basham SE, Padovani C, Lou Y, et al. Prospective discovery of small molecule enhancers of an E3 ligase-substrate interaction. Nat Commun. 2019;10:1402. doi:10.1038/s41467-019-09358-9.

21. Treier M, Staszewski LM, Bohmann D. Ubiquitin-dependent c-Jun degradation in vivo is mediated by the delta domain. Cell. 1994;78:787–798. doi:10.1016/S0092-8674(94)90502-9.

22. Wei W, Jin J, Schlisio S, Harper JW, Kaelin WG Jr. The v-Jun point mutation allows c-Jun to escape GSK3-dependent recognition and destruction by the Fbw7 ubiquitin ligase. Cancer Cell. 2005;8:25–33. doi:10.1016/j.ccr.2005.06.005.

23. Nateri AS, Riera-Sans L, Da Costa C, Behrens A. The ubiquitin ligase SCFFbw7 antagonizes apoptotic JNK signaling. Science. 2004;303:1374–1378. doi:10.1126/science.1092880.

24. Welcker M, Clurman BE. FBW7 ubiquitin ligase: a tumour suppressor at the crossroads of cell division, growth and differentiation. Nat Rev Cancer. 2008;8:83–93. doi:10.1038/nrc2290.

25. Morton S, Davis RJ, McLaren A, Cohen P. A reinvestigation of the multisite phosphorylation of the transcription factor c-Jun. EMBO J. 2003;22:3876–3886. doi:10.1093/emboj/cdg388.

26. van Dam H, Duyndam M, Rottier R, Bosch A, de Vries-Smits L, Herrlich P, et al. Heterodimer formation of cJun and ATF-2 is responsible for induction of c-jun by the 243 amino acid adenovirus E1A protein. EMBO J. 1993;12:479–487. doi:10.1002/j.1460-2075.1993.tb05680.x.

27. Hess J, Angel P, Schorpp-Kistner M. AP-1 subunits: quarrel and harmony among siblings. J Cell Sci. 2004;117:5965–5973. doi:10.1242/jcs.01589.

28. Eferl R, Wagner EF. AP-1: a double-edged sword in tumorigenesis. Nat Rev Cancer. 2003;3:859–868. doi:10.1038/nrc1209.

29. Papavassiliou AG, Musti AM. The multifaceted output of c-Jun biological activity: focus at the junction of CD8 T cell activation and exhaustion. Cells. 2020;9:2470. doi:10.3390/cells9112470.

30. Chen L, Glover JNM, Hogan PG, Rao A, Harrison SC. Structure of the DNA-binding domains from NFAT, Fos and Jun bound specifically to DNA. Nature. 1998;392:42–48. doi:10.1038/32100.

31. Cowan AD, Ciulli A. Driving E3 ligase substrate specificity for targeted protein degradation: lessons from nature and the laboratory. Annu Rev Biochem. 2022;91:295–319. doi:10.1146/annurev-biochem-032620-104421.

32. Tang Y, Chen Z, Zuo Q, Kang Y. Regulation of CD8+ T cells by lipid metabolism in cancer progression. Cell Mol Immunol. 2024;21:1215–1230. doi:10.1038/s41423-024-01224-z.

33. Wherry EJ, Kurachi M. Molecular and cellular insights into T cell exhaustion. Nat Rev Immunol. 2015;15:486–499. doi:10.1038/nri3862.

34. Pauken KE, Sammons MA, Odorizzi PM, Manne S, Godec J, Khan O, et al. Epigenetic stability of exhausted T cells limits durability of reinvigoration by PD-1 blockade. Science. 2016;354:1160–1165. doi:10.1126/science.aaf2807.

Figure legends

Figure 1. Fecal DHLCA is elevated in patients with colorectal cancer and is associated with disease progression.

(A) Workflow for fecal sample processing, targeted LC-MS/MS analysis, peak integration, and bile acid quantification.

(B) Relative abundance of the 18 bile acid features detected in >80% of the combined cohort (77 patients with CRC and 29 healthy donors), visualized after log10(x + 1) transformation. Multiple testing was controlled using the Benjamini-Hochberg false-discovery-rate procedure.

(C) Fecal DHLCA concentrations in patients with CRC and healthy donors.

(D–G) Fecal DHLCA concentrations in patients with CRC stratified by tumor invasion depth (T1–T2 versus T3–T4), lymph node status (N0 versus N1–N2), distant metastasis (M0 versus M1), and TNM stage (I–II versus III–IV), respectively.

Data in (C–G) are shown as individual values with mean ± SD; each point represents one participant. Two-group comparisons were performed using two-sided Mann-Whitney U tests. For bile acid profiling in (B), P values were adjusted using the Benjamini-Hochberg method. See also Figure S1 and Tables 1 and S1.

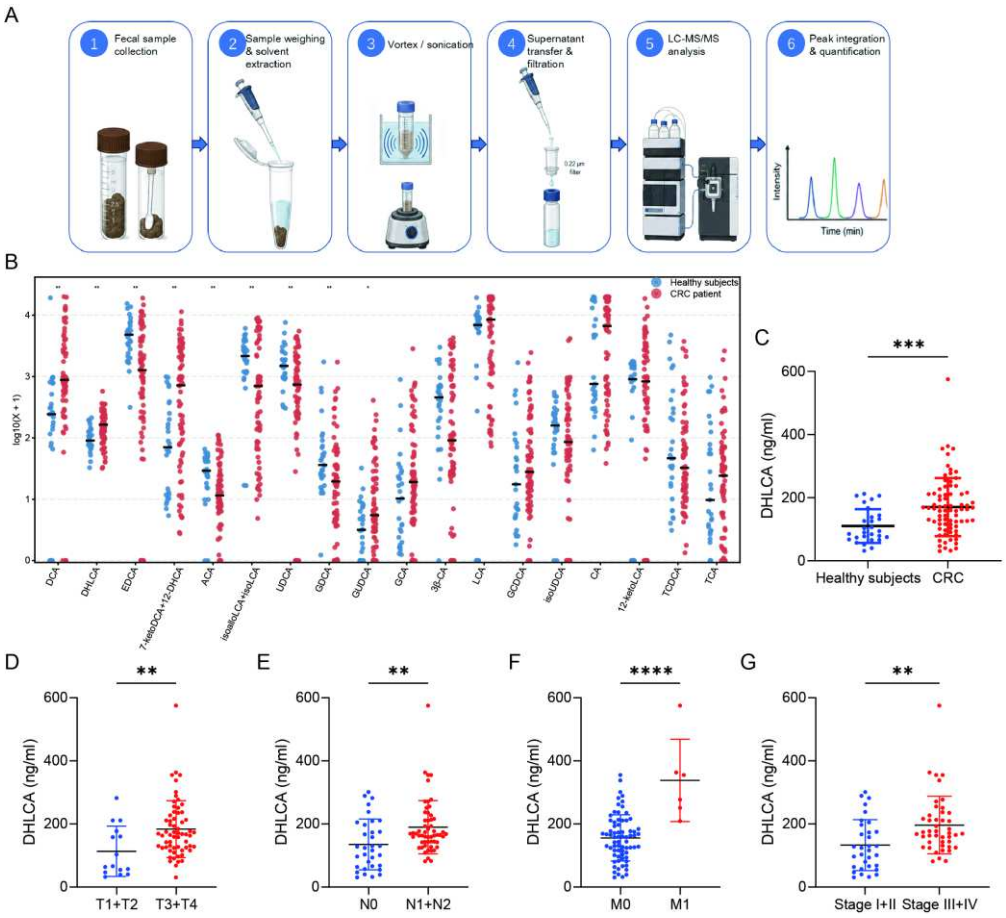


Figure 2. DHLCA promotes colorectal tumor growth through a CD8⁺ T cell-dependent mechanism.

(A) Experimental design for the MC38 syngeneic tumor model. C57BL/6J mice were inoculated subcutaneously with 1×10^6 MC38 cells; oral vehicle or DHLCA (10 mg/kg once daily) was initiated on day 1 after tumor inoculation.

(B) Representative excised MC38 tumors from vehicle- and DHLCA-treated mice. (C) Longitudinal tumor-growth curves. (D) Terminal tumor weight.

(E and F) Flow-cytometric analysis of $CD8^+$ and $CD4^+$ T cell frequencies in tumors and tumor-draining lymph nodes, respectively. (G–I) Tumor-associated macrophage, B cell, and NK cell frequencies. (J–L) Macrophage, B cell, and NK cell frequencies in tumor-draining lymph nodes.

(M) Experimental design for $CD8^+$ T cell depletion. MC38-bearing mice received vehicle or DHLCA together with anti-CD8α depleting antibody or isotype control (200 μg intraperitoneally on days −6, +1, and +8 relative to tumor inoculation). Oral vehicle or DHLCA treatment began on day 1.

(N) Flow-cytometric validation of $CD8^+$ T cell depletion.

(O) Representative excised tumors from the four CD8-depletion treatment groups. (P) Longitudinal tumor-growth curves. (Q) Terminal tumor weight.

Mouse experiments used n = 6 mice per group. Longitudinal tumor-growth data were analyzed by two-way repeated-measures ANOVA when complete repeated measurements were available and by mixed-effects modeling when values were missing. Endpoint and flow-cytometric comparisons were analyzed as indicated in the figure and Materials and methods. Data are shown as mean ± SD unless otherwise indicated. See also Figure S2.

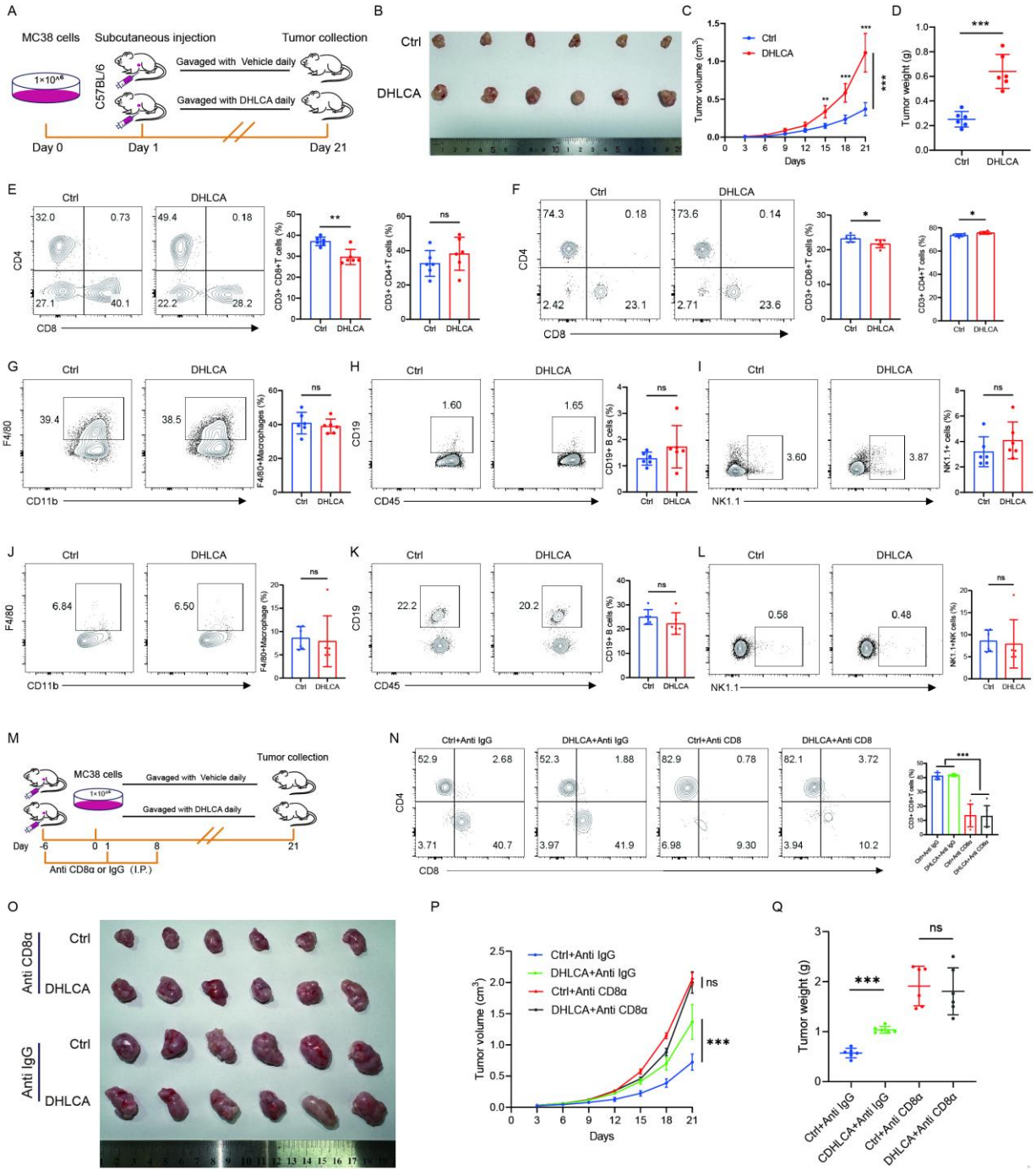


Figure 3. DHLCA suppresses CD8⁺ T cell proliferation, effector molecule production, and antigen-specific killing.

(A) Experimental workflow for primary mouse $CD8^+$ T cell isolation and activation. For 6-day functional assays, cells received anti-CD3/anti-CD28 plus IL-2 during days 0–3 and IL-2 plus IL-7 during days 3–6, with DHLCA maintained throughout treatment.

(B) Annexin V/propidium iodide analysis of MC38-OVA target-cell apoptosis after 24 h of co-culture with vehicle- or DHLCA-pretreated OT-1 cells; the adjacent graph quantifies target-cell apoptosis.

(C and D) Proliferation-associated flow-cytometric readouts after 72 h of treatment with 0, 20, or 40 μM DHLCA, shown as CFSE mean fluorescence intensity (MFI) and Ki-67 MFI, respectively.

(E and F) Frequencies of $GzmB^+$ and IFN-γ^+ $CD8^+$ T cells, respectively, after 6 days of culture followed by PMA/ionomycin restimulation.

(G and H) Frequencies of T-bet^+ and $Eomes^+$ $CD8^+$ T cells, respectively.

(I and J) Frequencies of $GzmB^+$ and IFN-γ^+ OT-1 $CD8^+$ T cells, respectively, after DHLCA treatment.

All experiments were performed independently three times (n = 3 independent biological experiments). Bar graphs show mean ± SD, and points represent independent biological replicates. One-factor comparisons were analyzed by one-way ANOVA followed by Tukey's multiple-comparisons test. See also Figure S3.

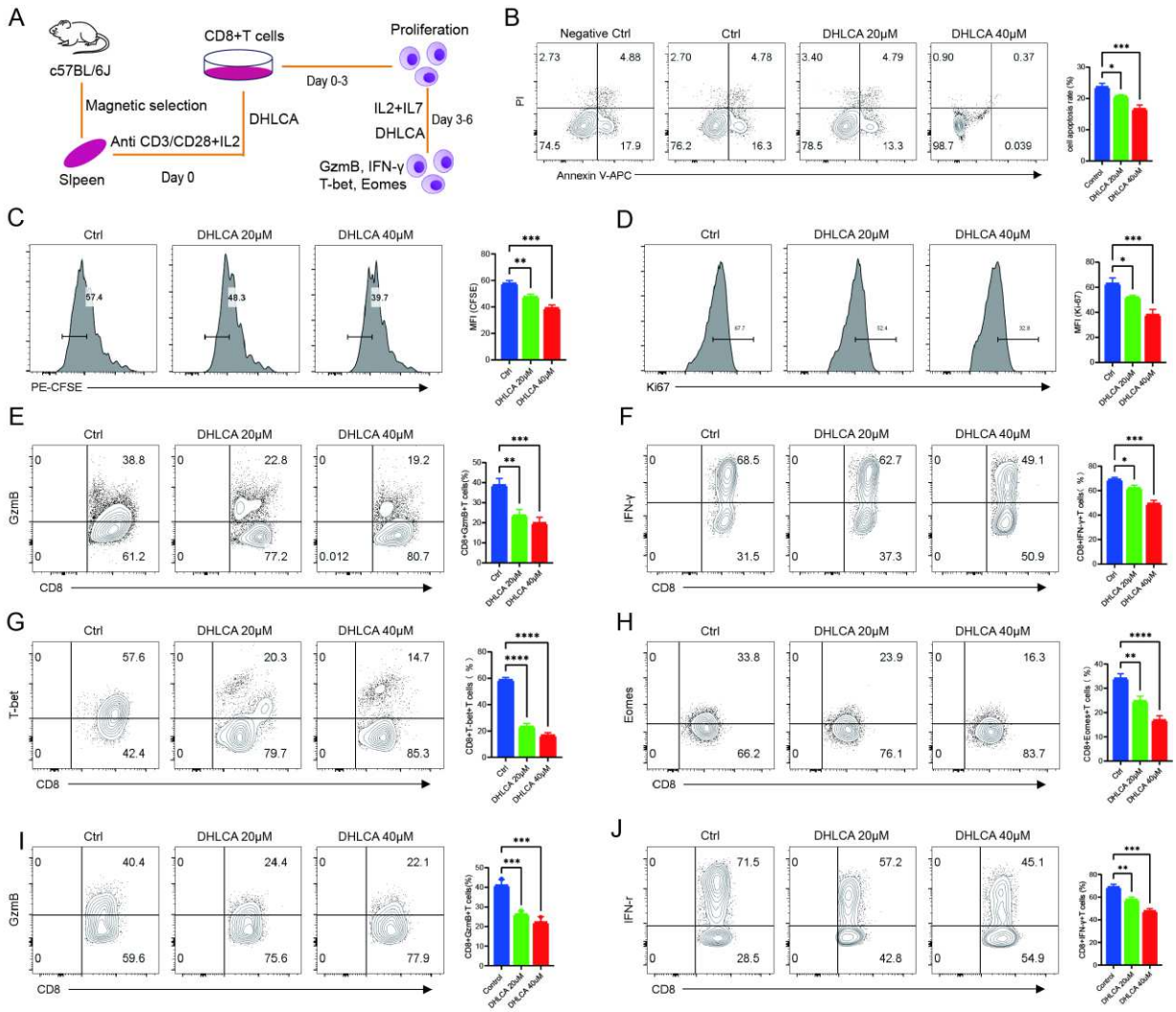


Figure 4. DHLCA reduces Jun transcript abundance, destabilizes c-Jun, and impairs AP-1-dependent transcription of Gzmb and Ifng.

(A) Cross-species integration of 24 human orthologs derived from the 42 exploratory mouse RNA-seq candidates with 753 genes differentially expressed between tumor-derived and normal-tissue-derived human CRC $CD8^+$ T cells, yielding 10 concordantly altered genes. Border-region samples were not included in this differential-expression comparison.

(B) Dose-response qPCR validation of the 10 concordant candidate genes after 72 h treatment with 0, 20, or 40 μM DHLCA; additional time-course validation is shown in Figures S4D and S4E.

(C) Immunoblot analysis of total JNK, phospho-JNK, c-Fos, total c-Jun, and phospho-c-Jun in activated $CD8^+$ T cells treated with 0, 20, or 40 μM DHLCA.

(D) Cycloheximide-chase immunoblot analysis of c-Jun decay. $CD8^+$ T cells were pretreated with vehicle or 40 μM DHLCA for 24 h, followed by 50 μM cycloheximide, and collected at 0, 2, 4, 6, and 8 h.

(E) Effect of proteasome inhibition with 10 μM MG132 on DHLCA-induced c-Jun loss.

(F) Ubiquitin immunoreactivity in c-Jun immunoprecipitates from activated $CD8^+$ T cells treated with 10 μM MG132 and 10 μM PR-619 for 6 h before c-Jun immunoprecipitation.

(G) Co-immunoprecipitation analysis of c-Jun-c-Fos complex formation using c-Fos immunoprecipitation, with matched IgG and input controls.

(H) Schematic of the candidate TRE-containing regulatory regions analyzed in Ifng and Gzmb.

(I–K) c-Jun ChIP analysis at Gzmb site 1, Gzmb site 2, and the Ifng TRE-containing region, respectively, showing representative endpoint PCR products and qPCR enrichment expressed as percentage of input.

(L and M) Dual-luciferase assays for Gzmb and Ifng promoter reporters, respectively. HEK293T cells were co-transfected with wild-type or TRE-mutant firefly reporters, Renilla normalization vector, and empty vector or c-Jun expression plasmid; firefly activity was normalized to Renilla and expressed relative to the corresponding vector control.

Cell-based validation experiments were performed independently three times. Routine immunoblots in (C–G) are representative of three independent experiments and were not

subjected to densitometric band quantification. qPCR, ChIP-qPCR, and dual-luciferase data represent n = 3 independent biological experiments and are shown as mean ± SD. Dual-luciferase data were analyzed by two-way ANOVA with reporter genotype and c-Jun expression as factors and Šídák-adjusted planned comparisons. Statistical tests for the remaining quantified panels are indicated in the figure and Materials and methods. See also Figure S4 and Tables S2 and S3.

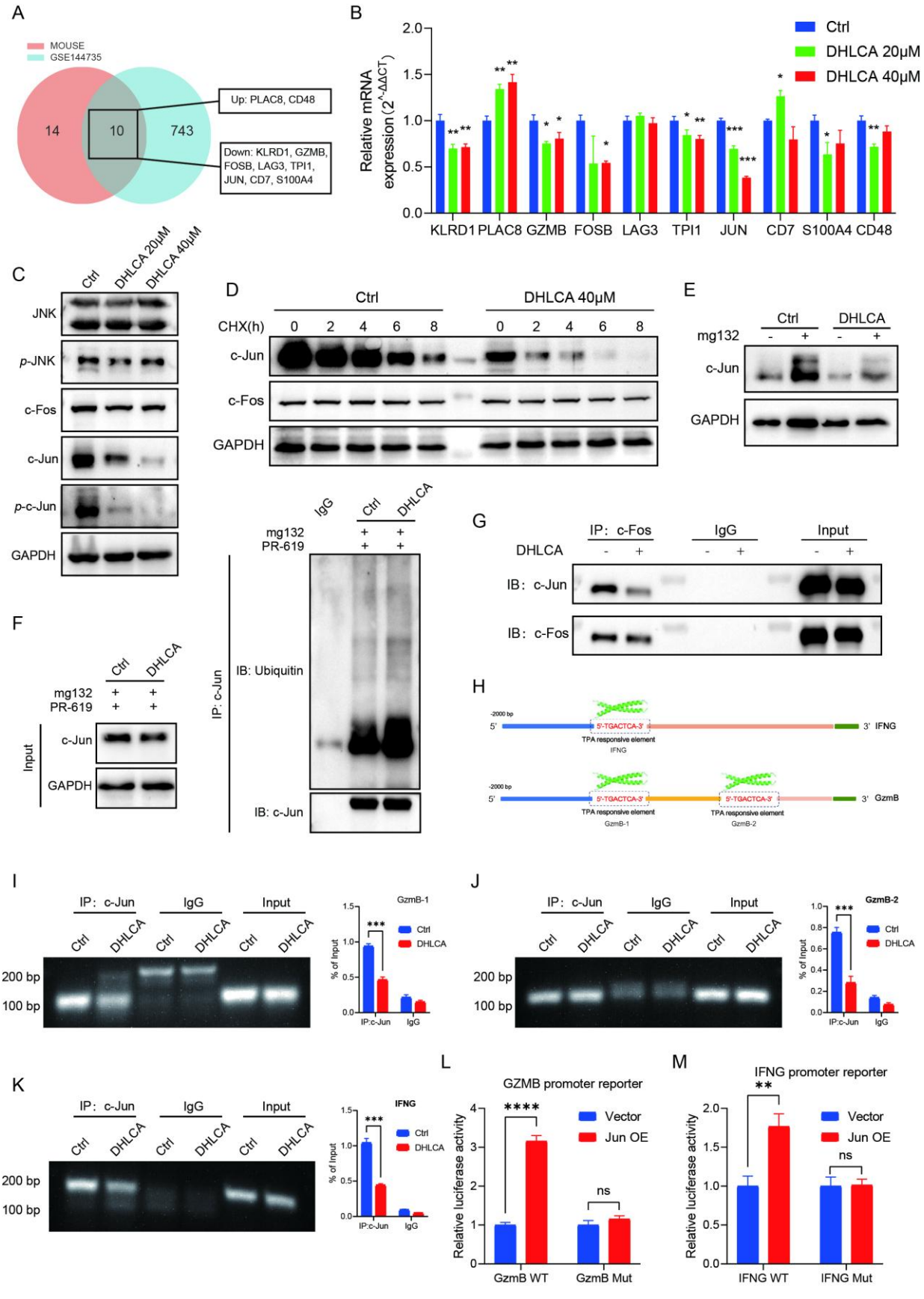

A
MOUSE
GSE144735
14
10
743
Up: PLAC8, CD48
Down: KLRD1, GZMB, FOSB, LAG3, TPI1, JUN, CD7, S100A4
B
Relative mRNA expression (2^-ΔΔCT)
Ctrl
DHLCA 20μM
DHLCA 40μM
KLRD1 PLAC8 GZMB FOSB LAG3 TPI1 JUN CD7 S100A4 CD48
C
Ctrl
DHLCA 20μM
DHLCA 40μM
JNK
p-JNK
c-Fos
c-Jun
p-c-Jun
GAPDH
D
Ctrl
DHLCA 40μM
CHX(h) 0 2 4 6 8 0 2 4 6 8
c-Jun
c-Fos
GAPDH
E
Ctrl
DHLCA
mg132
c-Jun
GAPDH
F
Ctrl
DHLCA
mg132
PR-619
Input
c-Jun
GAPDH
IgG
Ctrl
DHLCA
mg132
PR-619
IP: c-Jun
IB: Ubiquitin
IB: c-Jun
G
IP: c-Fos
IgG
Input
DHLCA
IB: c-Jun
IB: c-Fos
H
-2000 bp
5'
5'-TGACTCA-3'
3' IFNG
TPA responsive element
IFNG
-2000 bp
5'
5'-TGACTCA-3'
5'-TGACTCA-3'
3' GzmB
TPA responsive element
TPA responsive element
GzmB-1
GzmB-2
I
IP: c-Jun
IgG
Input
Ctrl
DHLCA
200 bp
100 bp
GzmB-1
% of Input
IP:c-Jun
IgG
J
IP: c-Jun
IgG
Input
Ctrl
DHLCA
200 bp
100 bp
GzmB-2
% of Input
IP:c-Jun
IgG
K
IP: c-Jun
IgG
Input
Ctrl
DHLCA
200 bp
100 bp
IFNG
% of Input
IP:c-Jun
IgG
L
GZMB promoter reporter
Vector
Jun OE
Relative luciferase activity
GzmB WT
GzmB Mut
M
IFNG promoter reporter
Vector
Jun OE
Relative luciferase activity
IFNG WT
IFNG Mut

Figure 5. Forced c-Jun expression partially restores CD8$^+$ T cell effector function suppressed by DHLCA.

(A) Immunoblot analysis of JNK, phospho-JNK, c-Fos, c-Jun, and phospho-c-Jun in primary mouse CD8$^+$ T cells transduced with empty-control or c-Jun-IRES-EGFP retrovirus and cultured with vehicle or 40 μM DHLCA.

(B and C) Frequencies of GzmB$^+$ and IFN-γ$^+$ CD8$^+$ T cells, respectively, after transduction with empty-control or c-Jun retrovirus and culture with vehicle or DHLCA.

(D) Annexin V/propidium iodide analysis of MC38-OVA target-cell apoptosis after co-culture with vehicle- or DHLCA-pretreated OT-1 cells transduced with empty-control or c-Jun retrovirus.

(E) LDH-based cell-killing rate under the same conditions as in (D).

All experiments were performed independently three times (n = 3 independent biological experiments). The immunoblot in (A) is representative of three independent experiments and was not subjected to densitometric band quantification. Quantified functional assays in (B–E) are shown as mean ± SD. Two-factor comparisons were analyzed by two-way ANOVA with Šídák-adjusted planned comparisons, as specified in the figure and Materials and methods. See also Figure S5.

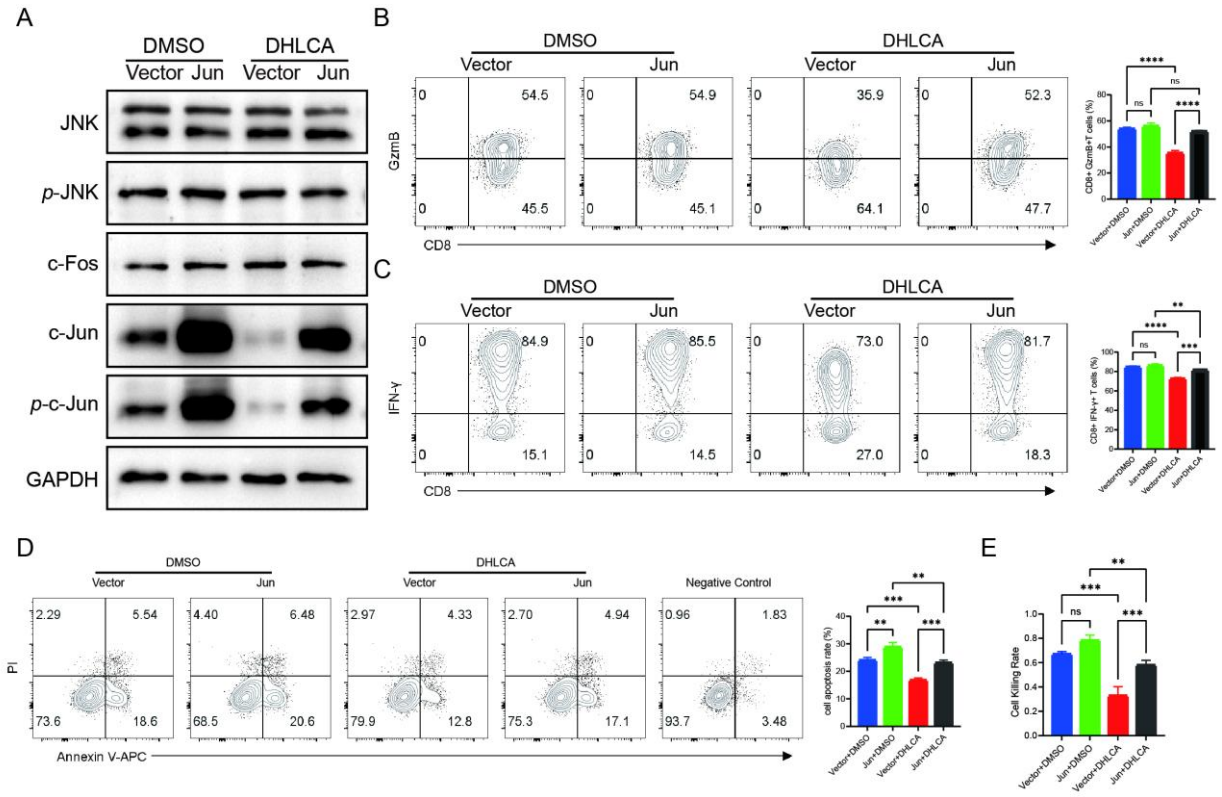


Figure 6. A distal pocket in FBW7 contributes to DHLCA-enhanced FBW7-c-Jun recognition.

(A) Immunoblot analysis of FBW7 and c-Jun in activated primary mouse $CD8^+$ T cells treated with vehicle or 40 μM DHLCA for 72 h. Where indicated, MG132 (10 μM) was added during the final 6 h before collection.

(B) c-Jun immunoprecipitation followed by FBW7 immunoblotting to assess endogenous FBW7-c-Jun association after 72 h of vehicle or 40 μM DHLCA exposure. MG132 (10 μM) was added during the final 6 h where indicated. Matched IgG and input controls are shown.

(C) Molecular-docking model of DHLCA within the structured core of FBW7, with an enlarged view of the predicted distal pocket and representative predicted contacts.

(D and E) Lysate-based thermal-shift analysis of wild-type FBW7 and the six-site alanine pocket mutant (I330A/D331A/R357A/K590A/F632A/N668A), respectively. HEK293T lysates

expressing the indicated Flag-FBW7 construct were incubated with vehicle or 40 μM DHLCA for 2 h and subsequently heated at 49, 52, 55, 58, 61, or 64°C for 20 min before analysis of residual soluble FBW7.

(F and G) Reconstituted FBW7-c-Jun interaction in HEK293T cells co-expressing c-Jun with wild-type or six-site alanine-mutant Flag-FBW7, respectively. Cells were exposed to vehicle or 40 μM DHLCA for 24 h, with MG132 (10 μM) and PR-619 (10 μM) added during the final 6 h before Flag immunoprecipitation and c-Jun immunoblotting.

(H and I) c-Jun abundance in HEK293T cells expressing wild-type or six-site alanine-mutant Flag-FBW7, respectively, after 24 h of vehicle or 40 μM DHLCA treatment.

Cell-based biochemical experiments were independently repeated three times. Routine immunoblots are representative of three independent experiments. The relative soluble-FBW7 profiles in (D and E) are displayed as shown in the figure; statistical analyses for these profiles and any other quantified readouts are specified in the figure and Materials and methods.

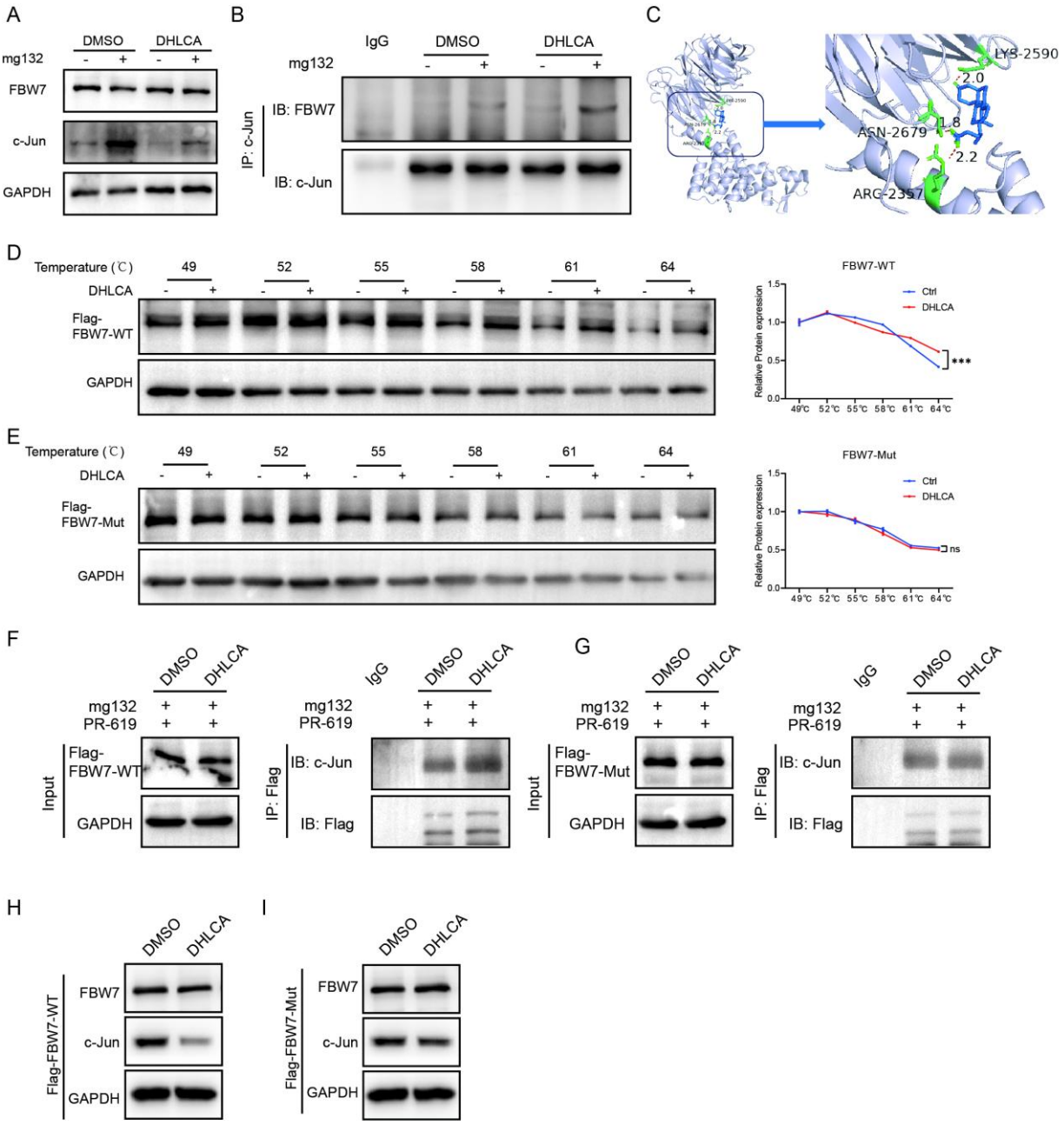


Figure 7. DHLCA suppresses c-Jun-dependent CD8⁺ T cell immunity *in vivo* and recapitulates effector suppression in human CD8⁺ T cells.

(A) Experimental design for adoptive transfer in the MC38-OVA model. C57BL/6J recipients were inoculated with 2 × 10^6 MC38-OVA cells. CD45.1⁺ OT-1 CD8⁺ T cells were transduced with empty-control or c-Jun expression vectors, exposed ex vivo to vehicle or DHLCA, and transferred intravenously (1 × 10^6 cells per mouse) on days 7 and 14.

(B) Representative excised MC38-OVA tumors after adoptive transfer. (C) Terminal tumor weight. (D) Longitudinal tumor-growth curves.

(E) Experimental design for combined DHLCA exposure and PD-1 blockade in the MC38 model. Oral vehicle or DHLCA (10 mg/kg once daily) was initiated on day 1; anti-PD-1 antibody or isotype control (200 μg intraperitoneally) was administered on days 7 and 14.

(F) Representative excised MC38 tumors. (G) Terminal tumor weight. (H) Longitudinal tumor-growth curves under isotype-control or anti-PD-1 treatment with vehicle or DHLCA.

(I) Experimental design for chronic dietary DHLCA exposure in male $Apc^{Min/+}$ mice. Treatment was initiated at 6 weeks of age and formulated to provide an estimated exposure of approximately 10 mg/kg/day through 120 days of age or until humane endpoints were reached.

(J) Representative colons showing grossly visible lesions. (K) Number of grossly visible colonic lesions at endpoint (control diet, n = 7; DHLCA diet, n = 8).

(L) Kaplan-Meier survival analysis of control-diet (n = 7) and DHLCA-diet (n = 8) $Apc^{Min/+}$ mice.

(M) Experimental design for paired ex vivo analysis of human PBMCs from 12 healthy donors. PBMCs were activated with anti-CD3/anti-CD28 and IL-2 during days 0–3, then maintained with IL-2 and IL-7 during days 3–6; vehicle or 40 μM DHLCA was present throughout the 6-day culture period.

(N) Paired frequency of $CD8^+$ T cells within the $CD3^+$ T cell compartment.

(O and P) Paired frequencies of $GzmB^+$ and IFN-γ^+ human $CD8^+$ T cells, respectively, after restimulation.

(Q) c-Jun expression in human $CD8^+$ T cells, quantified as mean fluorescence intensity (MFI).

Adoptive-transfer and anti-PD-1 experiments used n = 6 mice per group. The $Apc^{Min/+}$ diet experiment used n = 7 mice in the control-diet group and n = 8 mice in the DHLCA-diet group.

Longitudinal tumor-growth data were analyzed by two-way repeated-measures ANOVA when complete repeated measurements were available and by mixed-effects modeling when values were missing. Survival was compared using the log-rank test. Paired human PBMC comparisons were analyzed using paired tests as specified in Materials and methods; n = 12 donors and each paired line represents one donor. Data are shown as mean ± SD unless otherwise indicated. See also Figure S6.

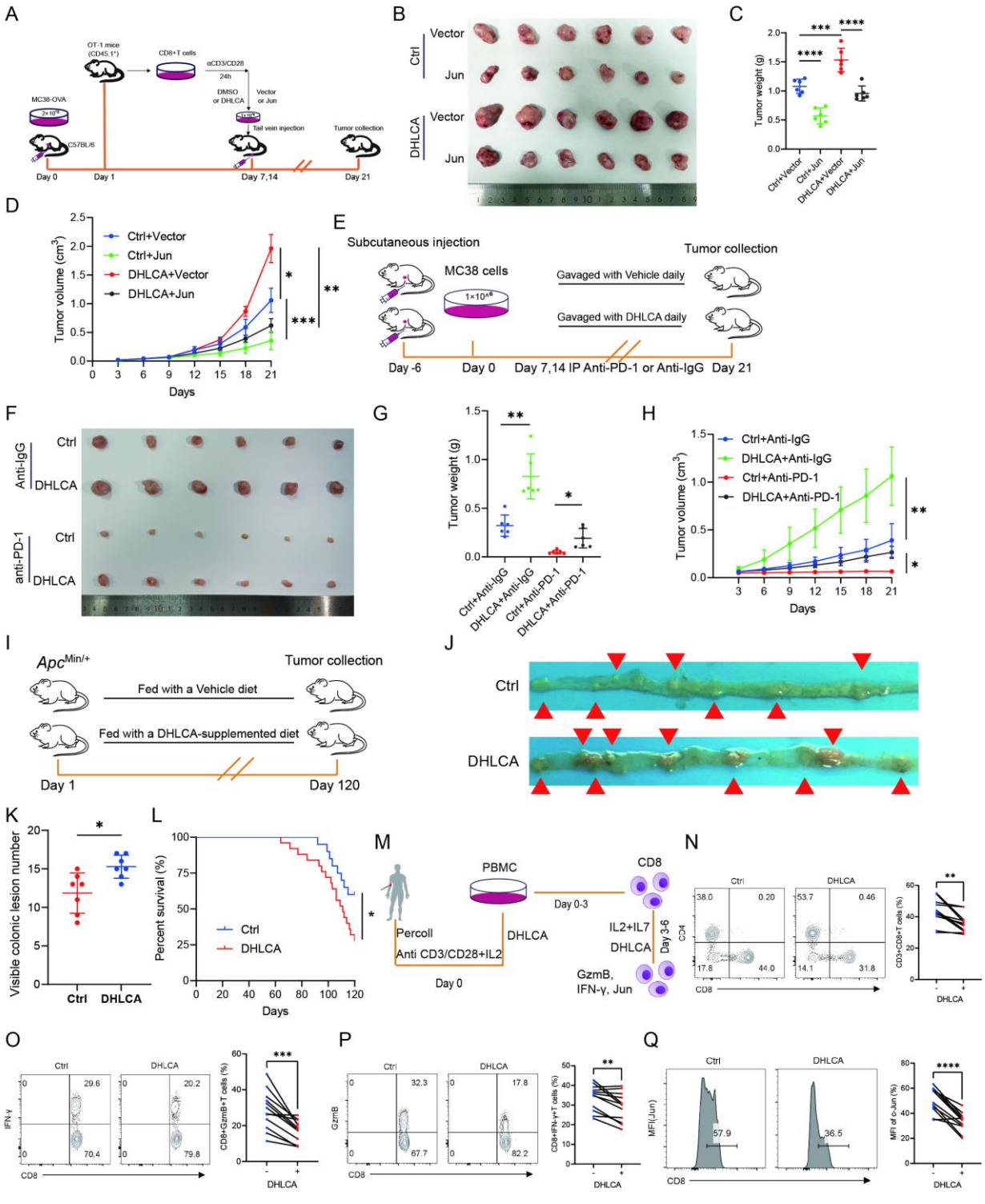

A
OT-1 mice (CD45.1+)
CD8+T cells
αCD3/CD28
24h
DMSO or DHLCA
Vector or Jun
MC38-OVA
C57BL/6
Tail vein injection
Tumor collection
Day 0
Day 1
Day 7,14
Day 21
B
Ctrl
Vector
Jun
DHLCA
Vector
Jun
C
Tumor weight (g)
Ctrl+Vector
Ctrl+Jun
DHLCA+Vector
DHLCA+Jun
D
Tumor volume (cm3)
Ctrl+Vector
Ctrl+Jun
DHLCA+Vector
DHLCA+Jun
Days
E
Subcutaneous injection
MC38 cells
Tumor collection
Gavaged with Vehicle daily
Gavaged with DHLCA daily
Day -6
Day 0
Day 7,14 IP Anti-PD-1 or Anti-IgG
Day 21
F
Anti-IgG
Ctrl
DHLCA
anti-PD-1
Ctrl
DHLCA
G
Tumor weight (g)
Ctrl+Anti-IgG
DHLCA+Anti-IgG
Ctrl+Anti-PD-1
DHLCA+Anti-PD-1
H
Tumor volume (cm3)
Ctrl+Anti-IgG
DHLCA+Anti-IgG
Ctrl+Anti-PD-1
DHLCA+Anti-PD-1
Days
I
Apc Min/+
Tumor collection
Fed with a Vehicle diet
Fed with a DHLCA-supplemented diet
Day 1
Day 120
J
Ctrl
DHLCA
K
Visible colonic lesion number
Ctrl
DHLCA
L
Percent survival (%)
Ctrl
DHLCA
Days
M
PBMC
Percoll
Anti CD3/CD28+IL2
DHLCA
Day 0
Day 0-3
CD8
IL2+IL7
DHLCA
Day 3-6
GzmB, IFN-γ, Jun
N
Ctrl
DHLCA
CD4
CD8
CD3+CD8+T cells (%)
DHLCA
O
Ctrl
DHLCA
IFN-γ
CD8
CD8+GzmB+T cells (%)
DHLCA
P
Ctrl
DHLCA
GzmB
CD8
CD8+IFN-γ+T cells (%)
DHLCA
Q
Ctrl
DHLCA
MFI(Jun)
CD8
MFI of c-Jun (%)
DHLCA

Table 1. Association between fecal DHLCA levels and clinicopathological characteristics in patients with colorectal cancer

Characteristic	Total, n	Fecal DHLCA level (n=77)		*P* [a]
		Low (n=38)	High (n=39)	
Age (years)				0.935
≤60	26	13	13	
>60	51	25	26	
Gender				0.707
Female	30	14	16	
Male	47	24	23	
Tumor diameter (cm)				0.310
≤5	59	31	28	
>5	18	7	11	
Depth of invasion				**0.038**
T1/T2	15	11	4	
T3/T4	62	27	35	
Lymph node metastasis				**0.030**
N0	33	21	12	
N1/N2	44	17	27	
Distant metastasis				**0.025**
M0	71	38	33	
M1	6	0	6	
TNM stage				**0.007**
I	12	10	2	
II	20	11	9	
III	39	17	22	
IV	6	0	6	
Differentiation				0.569
Middle/High	24	13	11	
Poor	53	25	28	

P-value [a] calculated using Pearson's chi-squared test or Fisher's exact test, as appropriate.

Patients were dichotomized into DHLCA-low and DHLCA-high groups according to the median fecal DHLCA concentration.

Supplementary Files

This is a list of supplementary files associated with this preprint. Click to download.

- SupplementaryMethods.docx
- TableS2PrimersandrecombinantDNAsequences.docx
- Originalwesternblots.docx
- Supplementarydata.docx
- TableS3BulkRNAseqdifferentialexpression.xlsx
- TableS1CRCclinicopathologicalcharacteristics.docx
- TableS4Bileacidreferencestandards.docx